Toward higher-power Li-ion batteries

Lakhdar, Yazid; Chen, Yongxiu; geary, harry; Houck, Maurits; Groombridge, Alexander; Slater, Peter; Kendrick, Emma

DOI:
10.1016/j.jpowsour.2023.233710

Document Version
Publisher's PDF, also known as Version of record

Citation for published version (Harvard):
Lakhdar, Y, Chen, Y, geary, H, Houck, M, Groombridge, A, Slater, P & Kendrick, E 2023, 'Toward higher-power Li-ion batteries: Unravelling kinetics and thermodynamics of MoNb12O33 vs. NMC622', *Journal of Power Sources*, vol. 588, 233710. https://doi.org/10.1016/j.jpowsour.2023.233710

Journal of Power Sources 588 (2023) 233710

Contents lists available at ScienceDirect

Journal of Power Sources

journal homepage: www.elsevier.com/locate/jpowsour

Toward higher-power Li-ion batteries: Unravelling kinetics and thermodynamics of $MoNb_{12}O_{33}$ *vs.* NMC622

Yazid Lakhdar [a], Yongxiu Chen [a], Harry Geary [b], Maurits E. Houck [b], Alexander S. Groombridge [b], Peter R. Slater [c], Emma Kendrick [a,*]

[a] School of Metallurgy and Materials, University of Birmingham, Edgbaston Birmingham, B15 2TT, UK
[b] Echion Technologies Ltd, 9 Cambridge South, West Way, Sawston, Cambridge, CB22 3FG, UK
[c] School of Chemistry, University of Birmingham, Edgbaston Birmingham, B15 2TT, UK

HIGHLIGHTS

- Insights into the diffusion kinetics and thermodynamics of $MoNb_{12}O_{33}$.
- Formation of an unstable/reversible SEI layer at the surface of $MoNb_{12}O_{33}$ above 1.0 V.
- Excellent capacity retention and rate performance in full cell up to 20C even at 0 °C.
- Diffusion and reaction rate limiting factors in an NMC622.||$Nb_{12}MoO_{33}$ full cell

ARTICLE INFO

Keywords:
Niobium oxide
GITT
EIS
Diffusion coefficient
Fast-charging anode
Parameterisation

ABSTRACT

Wadsley-Roth niobates are promising anode materials for high-power lithium-ion batteries. The kinetics and thermodynamics of Li-ion transport in $MoNb_{12}O_{33}$ (MNO) electrodes were investigated, and its performance in high-power cells alongside a $LiNi_{0.6}Mn_{0.2}Co_{0.2}O_2$ (NMC622) cathode were optimised. Electrodes and cells were designed with an areal capacity of 1.2 ± 0.2 mAh cm^2, 90 wt% active material, and a negative-to-positive capacity ratio of ~1.2. Galvanostatic intermittent titration techniques and electrochemical impedance spectroscopy (EIS) were employed to elucidate kinetic and thermodynamic electrochemical parameters. MNO exhibited an exchange current density of ~0.012–0.021 mA cm^{-2} and high lithium diffusion coefficients of ~10^{-9} cm^2 s^{-1} at 50 % state of charge (SOC) and 25 °C. Lithiation and delithiation rate tests in MNO||Li and NMC622||MNO cell configurations at 15 °C and 0 °C highlighted the exceptional rate performance. Rapid charging of full cells was achieved at all tested temperatures, with charging times of 3 min–75 % state of charge at 25 °C, 6 min at 15 °C, and 30 min at 0 °C. Notably, a 6-min charge (10C rate) at 0 °C still provided 50 % of the initial capacity. EIS at various SOC levels indicated the formation of an unstable or reversible solid electrolyte interphase (SEI) layer on the MNO anode at 70–100 % SOC.

1. Introduction

Electric vehicle (EV) sales are entering an age of exponential growth spearheaded by the announced targets from multiple governments to ban the sale of new petrol and diesel cars within 10–15 years [1]. Both the range and the charging speed of EVs have seen tremendous improvements since the first generations of the Tesla Roadster and the Nissan Leaf, with some high-end mass-produced EV models now able to go more than 400 miles on a single charge and to charge from 20 to 80 % in ~15 min using ultra-fast DC chargers. However, charging EVs at very high current rates may reduce significantly the capacity and cycle life of battery packs based on current Li-ion technologies, and there is still room to increase the charging speed to bring it closer to the time required to fill up an internal combustion engine car, i.e. 2–5 min, especially at low temperatures. Furthermore, portable electronics, drones, vertical take-off and landing aircrafts, and power tools also require rechargeable batteries with increased power densities for faster charging and higher power delivery, respectively.

Niobium oxides are an emergent class of anode materials that could represent one of the solutions to enable long-lasting high-power lithium-

* Corresponding author.
E-mail address: e.kendrick@bham.ac.uk (E. Kendrick).

https://doi.org/10.1016/j.jpowsour.2023.233710
Received 2 August 2023; Received in revised form 19 September 2023; Accepted 4 October 2023
Available online 21 October 2023

ion batteries for EVs, drones, portable electronics, and power tools [2]. These materials have a dominant Li^+ intercalation potential above 1.0 V (vs. Li^+/Li), which likely makes them safer and more stable than SEI-forming graphite anodes, whilst having a much higher theoretical capacity than competing high-voltage $Li_4Ti_5O_{12}$ (LTO) anodes [3].

The reversible intercalation of Li^+ ions in Wadsley-Roth niobium oxide phases was first demonstrated by Cava et al. in 1983 [4]. Wadsley-Roth crystallographic shear structures have open ReO_3-like channels that enable fast Li^+ diffusivity, combined with shear planes that provide excellent stability and reversibility [5]. In fact, the diffusion of Li^+ ions in Wadsley-Roth niobium oxides was found to proceed intrinsically faster than in other high-power battery materials such as LTO or $LiFePO_4$ (LFP). Furthermore, niobium oxides also tend to have a higher theoretical capacity than LTO thanks to the double Nb^{5+}/Nb^{4+} and Nb^{4+}/Nb^{3+} redox couples, and the potential to include other redox-active cations.

Since $TiNb_2O_7$ was demonstrated as an alternative anode in 2011 [6], a large number of Wadsley-Roth niobium oxide materials have been demonstrated as negative electrodes in Li-ion batteries in the last 10 years, such as $Ti_2Nb_4O_{14}$ [7], $Al_{0.5}Nb_{24.5}O_{62}$ [8], PNb_9O_{25} [9], $WNb_{12}O_{33}^{10}$, $GeNb_{18}O_{47}$ [11], $Cr_{0.5}Nb_{24.5}O_{62}$ [12], $AlNb_{11}O_{29}$, [13,14] and Nb_2O_5 [15].

However, there is still relatively little known in the literature about the kinetics and thermodynamics of Li-ion batteries based on niobium oxide anodes with real-world practical electrode compositions and design, particularly at low temperatures. The discharge rate for a $Al_{0.5}Nb_{24.5}O_{62}$-based full cell at 0 °C was investigated, but charging performance was not reported, and significant drop in capacity was observed. C/10, 1C, and 5C demonstrated a capacity of ~175, 125, and 75 mAh g^{-1}, respectively, at 0 °C [8]. $Nb_{16}W_5O_{55}$ demonstrated good cyclic stability in half-cell up to 404 cycles at low temperatures (0 and −20 °C) but was shown to experience significant specific capacity loss and poor rate performance at these lower temperatures [44]. The same niobium tungsten oxide (NWO) displayed again good cyclic stability in NMC622||NWO full cell but significant capacity loss at reduced temperature, with an ~22 % loss at 10 °C compared to 25 °C at 2C and as much as ~71 % less capacity at 10C [45].

Moreover, many investigations on niobium oxide anodes in the literature have reported highly impressive cycle life results and rate performance as high as 100C; however, in many cases the electrode design is often far from representative of real-world electrodes. These anode compositions often comprise only about 80 wt% active material, and sometime even as little as 65 wt% active material with 25 wt% conductive carbon additives – which in volume translates to as much as ~40 vol% of conductive carbons in these electrodes [8,12,16]. These high carbon content electrodes result in large capacitive contributions from the high surface area carbons, which overstate the electronic and ionic conductivity of these materials and significantly reduce practical energy density if used in a commercial Li-ion battery. Finally, the active mass loading of these electrodes is consistently between only 1 and 3 mg cm^{-2}, which can inflate the observed rate capability and cycling performance of these materials, compared to that in a more typical commercial electrode [8,16–19,44]

In this work, we attempt to provide a comprehensive understanding of the kinetics and thermodynamics of the Li-ion insertion/extraction processes in a modified $MoNb_{12}O_{33}$ negative electrode, optimised for power applications. Electrode coatings of 60–80 GSM were targeted, with a 90:5:5 wt/wt/wt ratio of active material, conductive carbon additives, and binder, respectively, corresponding to a volume ratio of approximately 78:11:11 v/v/v. Galvanostatic Intermittent Titration Technique (GITT) and Potentiostatic Electrochemical Impedance Spectroscopy (PEIS) at various temperatures were used to elucidate the kinetic and thermodynamic transport properties. Rate capability testing was also performed in half cells (MNO||Li) and in full cells (NMC622||MNO) at low temperatures (15 °C and 0 °C), and compared to the rate performance at 25 °C.

2. Experimental

2.1. Materials

The active anode material was a modified $MoNb_{12}O_{33}$ molybdenum-niobium oxide powder (MNO developmental material, Echion Technologies Ltd., UK). Some of the manufacturer's modifications to this niobium oxide material included doping and carbon-coating [20]. The cathode material was a commercial grade $Ni_{0.6}Mn_{0.2}Co_{0.2}O_2$ powder (NMC622, Targray, Canada). Carbon additives included carbon black powder (TIMCAL Super C45 or C65) and short carbon nanotubes (MWCNTs, NC7000, Nanocyl SA, Belgium). The binder was poly (vinylidene fluoride) (PVDF, Solvay). The current collector for both anode and cathode was a 16 μm thick battery grade aluminium foil.

The electrolyte used in all cells was a solution of 1 M $LiPF_6$ in 50:50 EC:DEC v/v (Sigma-Aldrich, Merck, U.K.). Lithium foil (PI-KEM) used as the counter electrode in half cells was rolled to ~70 μm thickness. A single 16 μm thick tri-layer polymer film (Celgard H1609) was used as the separator.

2.2. Materials characterisation

The average particle size dispersion of the raw MNO anode and NMC622 cathode powders was obtained by laser diffraction using a particle size analyser (Helos, Sympatec GmbH, Germany). A scanning electron microscope (TM3030+ Benchtop SEM, Hitachi, Japan) was used to observe the morphology of the raw active material powders. Cross-sections of the anode and cathode electrodes were obtained using a Hitachi Ion Milling System (IM4000 plus) at an accelerating voltage of 5 kV for 3 h. SEM images of pristine (non-cycled) electrode coatings were obtained at a working distance of 8 mm in an FEI Quanta SEM under an acceleration voltage of 15 and 20 kV for the cathode and anode, respectively. Cross-sections and raw powder images were analysed using an image processing software (ImageJ) to validate the average particle size measured by laser diffraction.

2.3. Electrodes and cells manufacturing

This work followed the detailed procedures for electrode slurry mixing and coating, as well as electrode calendering and cell building provided by Lakhdar et al. in a previous publication [21].

Briefly, anode and cathode electrodes consisted of 90 wt% active material, 5 wt% conductive carbons, and 5 wt% binder. The carbon additives ratio was 9:1 wt/wt carbon black/carbon nanotubes. First, a Thinky mixer was used to disperse the carbon additives in a PVDF/NMP solution. Active material powders were then progressively added to the mix (2000 rpm for 3min between each step). Both anode and cathode inks were coated onto 15 μm aluminium foil using a draw-down doctor blade (K Paint Applicator, RK Printcoat Instruments, U.K.) The mass loading of active materials in the electrodes was 6.0 ± 1.0 mg cm^{-2}. The volume fraction of active material in the electrodes was calculated from the porosity of the electrodes, which was determined from the thickness of the electrode coatings, the weight ratio of each material in the electrode composition, and the true density of each material. As the battery cells in this study were power-focused, the electrodes were coated to 1.2 ± 0.2 mAh cm^{-2}, which is similar to some electrode designs in some commercial high-power battery cells [22]. Electrode coatings were first dried at 80 °C on a hot plate and then transferred in a vacuum oven at 120 °C overnight. Calendering was performed on a hot rolling press (MSK-HRP-01, MTI Corporation, USA) at 80 °C to obtain the desired electrode thickness and density, targeting a porosity of 25–30 % based on electrode design optimisation from previous work [21]. Calendered coatings were then cut into individual electrode disks with a diameter of 14.8 mm and 15 mm for the cathode and anode, respectively. Full cells had a negative-to-positive capacity ratio of ~1.2 [21]. The entire preparation, from ink mixing and electrode coating to cell

manufacturing, was performed in a dry room (dew point −45 °C).

2.4. Electrochemical analysis

After cell assembly, a 12-h resting period was allowed for the electrolyte to fully soak the electrodes and separator. Cells first underwent two CC-CV charge - CC discharge formation cycles at 25 °C using a low current density of 10 mA g^{-1}. The current decay cut-off was set to 4 mA g^{-1} during the constant voltage step. Voltage windows were 1.1–2.5 V for MNO||Li anode half cells and 2.7–4.3 V for NMC622||Li cathode half cells, and 1.1–3.1 V for NMC622||MNO full cells. The rated capacity of the MNO and the NMC622, respectively, were determined from low rate cycles at 20 mA g^{-1} in half cells to be 210 mAh g^{-1} for the former and 175 mAh g^{-1} for the latter.

Electrochemical impedance spectroscopy was performed in potentiostatic mode (PEIS) on a VMP3 potentiostat (Biologic, France) at 0, 20, 40, 60, 80, and 100 % states of charge (SOC) using a C/10 charge for half cathode, half anode, and full cells. At each x% SOC, which were estimated by Coulomb counting, PEIS was performed after allowing a 30 min rest period to reach equilibrium. A frequency range of 10 mHz–400 kHz (with 10 points per decade) was applied with a 5 mV amplitude. For the data analysis, the ZFit function of the EC-Lab® software was used for the equivalent circuit models fitting. The tortuosity of battery electrodes has been shown to have a significant influence on the rate performance and cycling stability of lithium-ion cells [23]. PEIS was thus performed in symmetric cell setup, where two identical electrodes on current collector foil are placed either side of a separator in a coin cell using an ion-blocking electrolyte preventing insertion of the mobile ions, to calculate the tortuosity factor of the negative and positive electrodes [24–27].

Rate performance testing was performed for both lithiation and delithiation in lithium metal anode-half cells, and charge and discharge in full cells at 25, 15, and 0 °C.

For the positive electrode half-cell charge (delithiation) rate tests, a fixed CC-CV discharge (lithiation) was used with a constant current rate of C/2 and a C/20 current limit during the constant voltage step at 2.7 V. Then, variable nC (n = 0.1, 0.5, 1, 2, 5, 10, 20) CC delithiation charge rates were used in turn to respectively charge to 4.3 V vs. Li/Li^+. For lithiation rate testing, a fixed C/2 CC charge (delithiation) to 4.3 V vs. Li/Li^+ followed by a CV step to a current limit of C/20 was applied. Lithiation rates were tested to a 2.7 V vs. Li/Li^+ cut-off limit by using nC (n = 0.1, 0.5, 1, 2, 5, 10, 20) CC discharge rates. Similar rate tests were performed on the negative electrode, where fixed C/2 CC-CV lithiation and delithiation were performed to 1.1 V vs. Li/Li^+ and 2.5 V vs. Li/Li^+, respectively, and variable nC constant current delithiation and lithiation rates at nC (n = 0.1, 0.5, 1, 2, 5, 10, 20) were investigated.

In full cell configuration, charge and discharge was performed between 3.1 V and 1.0 V with the same current rates and temperatures as the MNO||Li half-cells. A summary of the cycling protocols is shown in Table S1 in *Supplementary Information*.

The galvanostatic intermittent titration technique (GITT) was performed in half coin cells at 25 °C to obtain the OCV and the apparent lithium diffusion coefficient (D_{Li}), Moreover, the series resistance obtained from PEIS measurements was subtracted from the DC-IR measured by GITT to calculate the charge transfer resistance (R_{ct}), from which the exchange current density (j_0) could then in turn be calculated. GITT was performed in the desired voltage window using a series 10 min current pulses at C/10 each followed by a 2.5 h resting period to ensure complete relaxation to OCV. Detailed explanations of the implications and limitations of GITT have already been provided elsewhere [28]. The diffusion coefficients extraction from GITT originated from the research work by Weppner and Huggins [29]. In this work, the Sand equation was used to fit the voltage transient during the current pulse as shown in Eq. (1) [28,30].

$$D_{Li^+} = \frac{4}{\pi}\left(\frac{iV_m}{nFS}\right)^2 \left(\frac{dE/d\delta}{dE/dt^{0.5}}\right)^2 \quad (1)$$

where i represents the current passing through the electrode in amps (A); V_m is the molar volume of active materials ($cm^3\ mol^{-1}$); n is the transferred electrons in reaction (n = 1); F is the Faraday constant ($C\ mol^{-1}$), and S is the active surface area between electrode and electrolyte (m^2). S is estimated from the average particle size of the active materials, and the thickness, coat weight, and porosity of the coatings, as in previous work [23]. $dE/d\delta$ is the slope of the coulometric titration curve, which is found by plotting the steady state voltages $E(V)$ measured after each titration step. $dE/dt^{0.5}$ is the slope of the linearized plot of the potential $E(V)$ during the current pulse. The stoichiometry in half cell was obtained using Eq. (2) at different SOCs:

$$Sto = \frac{C_{Li,x\%} \times \varepsilon_{ac} \times Th \times M}{GSM} \quad (2)$$

where $C_{Li,x\%}$ is the lithium concentration in the electrode ($mol\ m^{-3}$); ε_{ac} is the active material volume fraction; Th is the thickness of electrode material (m); M is the molar mass of active material ($g\ mol^{-1}$); GSM stands for grams per square meter and is the mass loading of active materials ($g\ m^{-2}$). The exchange current density j_0, expressed in $A\ m^{-2}$, reflects the rates of electron transfer as lithium ions migrate between the electrolyte and the electrode, was calculated from the R_{ct} obtained from GITT through the instantaneous voltage change $U(IR)$ when a current pulse is switched on or off. The IR drop is comprised of an ohmic overpotential and a charge-transfer overpotential ($\eta_{ohm}+\eta_{ct}$). The ohmic overpotential can be determined from the ohmic resistance ($\eta_{ohm} = R_s \times I$), where R_s is the series resistance, and I is the applied current. The overpotential relating to the charge-transfer in each pulse (η_{ct}) is obtained from Eq. (3).

$$\eta_{ct} = U(IR) - \eta_{ohm} \quad (3)$$

Finally, j_0 and R_{ct} are obtained from the linearization of the Butler-Volmer equation for small current densities, using the standard assumption that alpha – the charge-transfer coefficients for the anodic and cathodic directions of the half-reaction in electrode – is 0.5 for both the forward and backward reactions ($\alpha_a = \alpha_c = 0.5$) [31], as shown in Equation (4) through (6) [32].

$$j = j_0\left[\exp\left(\frac{\alpha_a F}{RT}\eta_{ct}\right) - \exp\left(-\frac{\alpha_c F}{RT}\eta_{ct}\right)\right] \quad (4)$$

$$j = \left[\frac{\alpha_a F}{RT}\eta_{ct} + \frac{\alpha_c F}{RT}\eta_{ct}\right] = j_0\frac{(\alpha_a + \alpha_c)F}{RT}\eta_{ct} \quad (5)$$

$$j_0 = \frac{RT}{F}\frac{j}{\eta_{ct}} = \frac{RT}{SF}\frac{1}{R_{ct}} \quad (6)$$

where R is the gas constant ($8.314\ J\ mol^{-1}\ K^{-1}$) and T is the temperature (298.15 K).

One study showed that the high rate performance of fast-charging battery electrodes is as much reaction rate-limited as it is diffusion-limited [33]. Reaction kinetics were found to be a critical rate-limiting parameter of the 20C charge performance of a H-phase Nb_2O_5 [15]. The reaction rate factor of the positive and negative electrodes in full cell were calculated from the exchange current density (j_0) obtained from PEIS analysis according to Equation (7), where k is the reaction rate ($A\ m^{-2}\ (m^3\ mol^{-1})^{1.5}$), whilst c_e and c_s are the electrolyte concentration and the lithium concentration in the host particle ($mol\ m^{-3}$), respectively [23].

$$k = \frac{j_0}{\sqrt{c_e c_s \left(c_s^{max} - c_s\right)}} \quad (7)$$

3. Results

3.1. Physical analysis

The particle size distribution of the MNO anode and NMC622 cathode powders were determined by combining SEM images of the raw active powders and electrode cross-sections, processed using ImageJ, with laser diffraction particle size analysis measurements. Results are shown in Fig. 1. The average particle diameter (D_{50}) approximated from SEM image processing for MNO and NMC622 was 2.5 and 9.9 μm, respectively, which were validated by the laser diffraction measurements that came in at 2.2 μm for MNO (Fig. 1e) and 10.1 μm for NMC622 (Fig. 1f). These values compared well with the literature for both MNO [8,16] and NMC [30,34]. As expected, NMC particles were found to be highly spherical (Fig. 1b) and their relatively large size resulted in the formation of large masses of conductive carbon powder in between NMC particles (Fig. 1d). On the other hand, the MNO powder was less spherical (Fig. 1a), although it was assumed to be spherical for the purpose of the GITT analysis. Its smaller particle size led to a more compact electrode microstructure with more point-to-point contact between active particles compared with the NMC, and a more evenly distributed network of carbon black throughout the electrode cross-section (Fig. 1c).

From PEIS of symmetric cells, shown in Fig. S1 in *Supplementary Information*, the tortuosity factor of the MNO and NMC622 electrodes used for rate testing was calculated at 1.68 and 1.36, respectively. Both of these tortuosity factors are relatively low due to the low thickness of these power-focused electrodes – 20 μm and 19 μm for negative and positive electrode, respectively. The slightly lower tortosity of the NMC electrode compared to the MNO electrode may be down to the much bigger average particle size of the NMC powder (Fig. 1f) combined with the low thickness of the electrode resulting in large carbon domains and pores between active particles (Fig. 1d) and providing relatively straightforward ionic pathways through the electrode microstructure.

The separator was a Celgard® H1609 tri-layer PP/PE/PP microporous membrane with a thickness of 16 μm and variable porosity between the different layers but a porosity of 50 % overall according to the manufacturer's specifications. The physical properties of the various cell components are summarised in Table 1.

The electrolyte we used in all battery cells in this work was a 1.0 M $LiPF_6$ in EC:DEC (1:1 v/v). The diffusion coefficient of lithium salts ($LiPF_6$ or $LiClO_4$) with a concentration of 0.1–2 mol dm^{-3} in typical liquid electrolyte carbonate solvents – such as EC:DEC, PC, or PC:EC:DEC – was consistently shown in the literature to range between 1×10^{-5} and 6×10^{-5} cm^2 s^{-1} at 25 °C [35]. In particular, electrolytes identical to the one used in the present work were determined to have a lithium diffusion coefficient of $2.2 \pm 0.5 \times 10^{-6}$ cm^2 s^{-1} (average of three independent studies) [36–38]. Furthermore, the ionic conductivity κ, thermodynamic factor (TDF), and cation transference number t_+ of this electrolyte were found to be approximately 0.8 S m^{-1}, 1.86, and 0.2, respectively [38].

3.2. Formation, GITT, and stoichiometry

First, the first two formation cycles of the MNO and NMC622 half cells, respectively, as well as of the NMC622||MNO full coin cell, all performed using a current density of 10 mA g^{-1}, are provided in Fig. S2 in *Supplementary Information*.

The Galvanostatic Intermittent Titration Technique (GITT), where a constant current pulse is applied for a set short duration followed by a

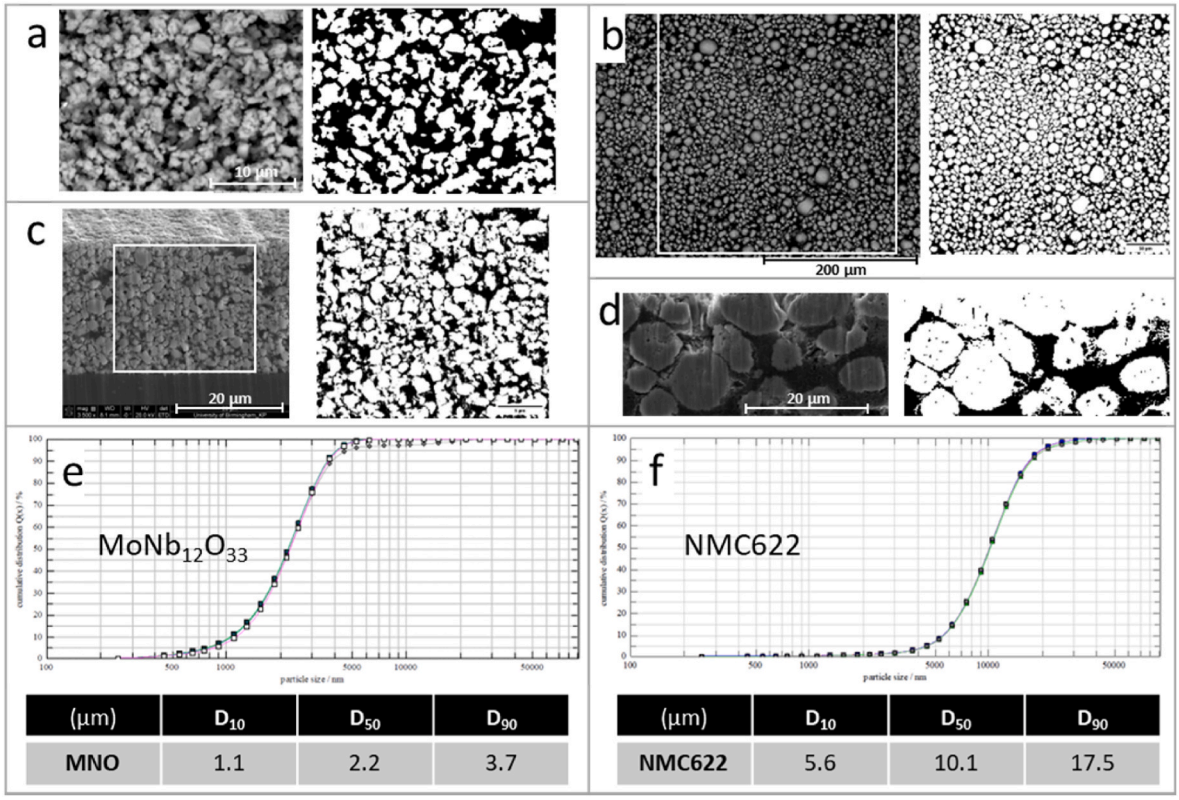

(μm)	D_{10}	D_{50}	D_{90}
MNO	1.1	2.2	3.7

(μm)	D_{10}	D_{50}	D_{90}
NMC622	5.6	10.1	17.5

Fig. 1. SEM images of the raw $MoNb_{12}O_{33}$ (a) and NMC622 (b) powders and the electrode cross-sections of the $MoNb_{12}O_{33}$ anode (c) and NMC622 cathode (d), each with their respective associated images processed using ImageJ for particle size determination, where active material particles are presented in white while pores and carbon domain are shown in black. Particle size distribution of the MNO (e) and NMC622 (f) powders from laser diffraction analysis.

Table 1
Physical characteristics of the materials, electrodes, and half-cells used in GITT experiments.

Negative Electrode Property		Positive Electrode Property	
MNO d_{50} (μm)	2.2	NMC622 d_{50} (μm)	10.1
MNO true density	4.62	NMC622 true density	4.78
MNO molar mass (g/mol)	1776	NMC622 M mass (g/mol)	96.94
MNO molar volume (cm^3/mol)	384.4	NMC622 M volume (cm^3/mol)	20.28
Areal capacity (mAh/cm^2)	1.2	Areal capacity (mAh/cm^2)	1.0
Active mass loading (mg/cm^2)	5.7	Active mass loading (mg/cm^2)	5.7
Thickness (μm)	20	Thickness (μm)	19
GSM	64	GSM	63
Porosity (%)	27	Porosity (%)	23
Active material volume fraction	0.57	Active volume fraction	0.59
Negative electrode diam. (mm)	15	Positive electrode diam. (mm)	14.8
Active surface area (cm^2)	54.94	Active surface area (cm^2)	11.78
Conductivity (S/m)	22	Conductivity (S/m)	12
Electrolyte		**Other cell components**	
$LiPF_6$ in electrolyte (mol/dm^3)	1	Al current collector thickness (μm)	15
Quantity of electrolyte in cells (mm^3)	70	Separator thickness (μm)	16
		Separator porosity (%)	50

longer rest period to reach OCV, was used to obtain the OCV, Stoichiometry, dQ/dV, and D_{Li} plots for both lithiation and delithiation, as well as the R_{ct} and j_0 plots. In these GITT tests of the negative and the positive electrodes half-cells, respectively, we applied a 20 mA g^{-1} current pulse for 10 min followed by a 2.5 h rest period to allow for complete relaxation.

Fig. 2 shows the GITT time plot (Fig. 2 a and 2.b) and capacity plot (Fig. 2c and 2d) for the $MoNb_{12}O_{33}$ anode half-cell between 1.0 and 2.2 V. A gravimetric capacity of ~230 mAh g^{-1} was obtained. The hysteresis – defined as the difference of open circuit potential between charge and discharge at a given state of charge – was found to be largest around 0 % and 50 % SOC (Fig. 2e). Increasingly bigger IR drops were also observed upon delithiation of the MNO, as increased polarisation above 2.2 V resulted in significantly higher overpotentials (Fig. 2f).

Fig. S3 in *Supplementary Information* shows the same GITT time and capacity plots for the NMC622 cathode half-cell between 2.7 and 4.3 V. A gravimetric capacity of ~175 mAh g^{-1} was obtained, with low hysteresis <40 mV at all SOCs (Fig. 3e) and bigger IR drops upon lithiation than delithiation (Fig. 3f).

The dQ/dV plot of the $MoNb_{12}O_{33}$ (Fig. 3a) is nearly identical to that of a $WNb_{12}O_{33}$ material of similar Wadsley-Roth shear ReO_3-type structure [10], albeit having its peaks shifted to slightly lower potentials, with a small oxidation peak at 1.11 V and a larger one at 1.70 V. The dQ/dV and stoichiometry plots of the NMC622||Li half-cell are shown in Fig. 3 b and Fig. 3 d, respectively, and are similar to results in the literature on the same material [30].

3.3. Diffusion coefficients

The apparent lithium solid phase diffusion coefficients D_{Li} in each active materials were determined by GITT from half-cells measurement. D_{Li} is essentially an effective diffusion coefficient as the transport properties are also affected by the mass loading of active material and the porosity [30]. The limitation of Li^+ diffusion in the electrode to the particle surfaces can be considered negated in GITT, because the diffusion coefficient is calculated from the equilibrium voltages, and therefore concentrations of lithium within the particles and in the electrolyte are assumed to be at equilibrium. Therefore, although the pore structure of the anode and cathode are extremely different at the particle level (Fig. 1); any contribution to the Li^+ transport from the electrolyte transport in the pore networks should be excluded as GITT was conducted at low current densities (0.1C).

Fig. 4 a shows that the apparent lithium diffusion coefficient of the $MoNb_{12}O_{33}$ anode $D_{Li/MNO}$ ranged between 2×10^{-11} and 1.2×10^{-9} $cm^2\ s^{-1}$, which is higher than that of the niobium oxides $TiNb_2O_7$ (10^{-15} $cm^2\ s^{-1}$) [39] and $NiNb_2O_6$ (10^{-12} $cm^2\ s^{-1}$) [40] reported in the literature, although it should be noted that despite it being common practice, comparing values of D_{Li} across studies is relatively difficult and inaccurate due to differences in measurement and analysis methods. Fig. 4 b shows that the diffusion coefficient of the NMC622 cathode $D_{Li/NMC}$ varied between 1×10^{-14} and 4×10^{-11} $cm^2\ s^{-1}$, which is consistent with values calculated for this material in the literature [25]. Therefore, D_{Li} of MNO was higher than that of NMC622 at all SOCs, during both lithiation and delithiation, thus highlighting the superior ionic

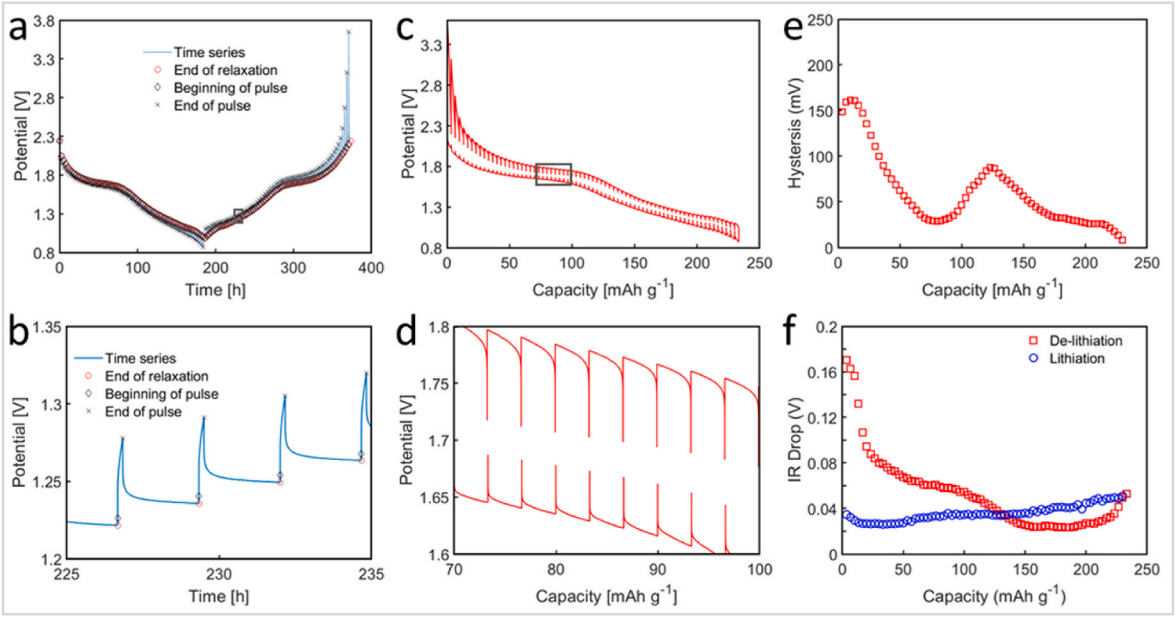

Fig. 2. GITT time plot for an $MoNb_{12}O_{33}$ anode half-cell (a) and close-up view highlighting the pulse and rest characteristics (b). GITT capacity plot (c) with close-up view (d), as well as potential hysteresis (e) and IR drops (f).

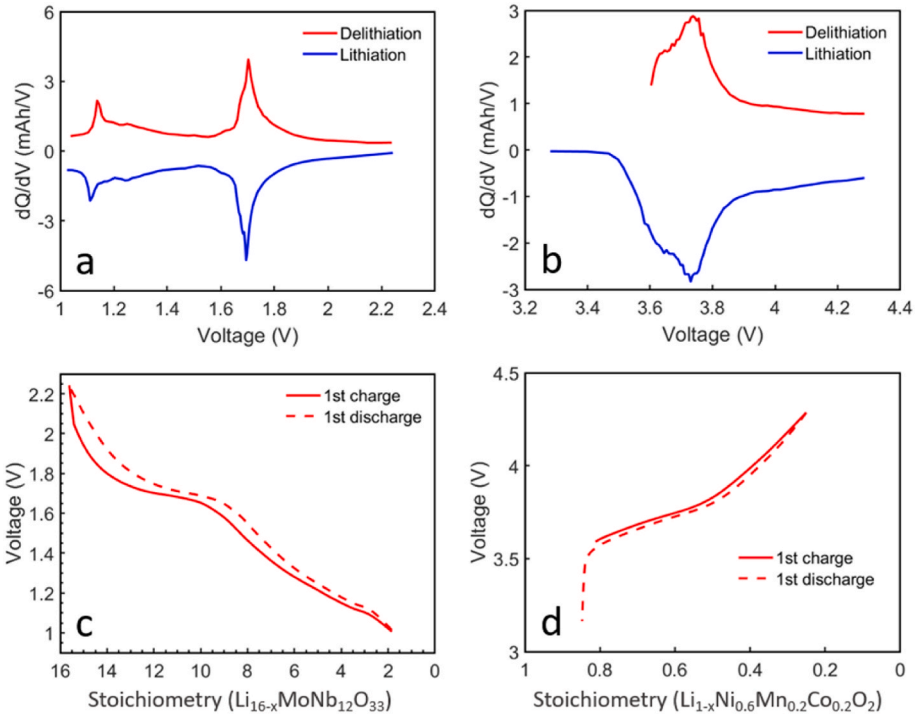

Fig. 3. dQ/dV plot for the $MoNb_{12}O_{33}$ anode half-cell (a) and $Ni_{0.6}Mn_{0.2}Co_{0.2}O_2$ cathode half-cell (b), and Stoichiometry plot for MNO (c) and NMC622 (b), calculated from GITT testing results.

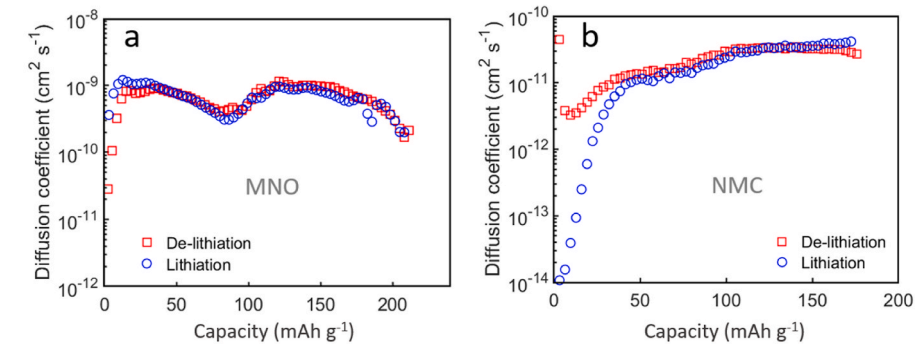

Fig. 4. Diffusion coefficient for MNO anode half-cell (a) and NMC 622 cathode half-cell (b) calculated from GITT testing results.

conductivity of $MoNb_{12}O_{33}$ and indicating that the cathode would be the diffusion-limiting electrode in NMC622||MNO full cells. This is a striking difference from the work that Chen et al. reported on an NMC622|| graphite system with comparable active mass loadings and similar GITT parameters and analysis [30]. In that case, it was the NMC622 that had the highest diffusion coefficient out of the two materials at most SOCs ($D_{Li/NMC} > D_{Li/graphite}$ at SOC >30 %) and the graphite anode was thus determined to be the diffusion rate-limiting electrode. This demonstrates the faster kinetics of this $MoNb_{12}O_{33}$ material over commercial graphite and explains in part its suitability for high-power battery storage applications.

3.4. Temperature dependence of electrode impedance

The exchange current density, j_0, and the charge transfer resistance, R_{ct}, were first calculated from the GITT analysis, and the resulting graphs of R_{ct} and j_0 at 25 °C are plotted in Fig. 5. The R_{ct} of the MNO||Li half-cell system (Fig. 5a) was found to be significantly higher than that of NMC622||Li (Fig. 5a), which is consistent with the overpotential issues reported in MNO||Li anode half-cells [21]. However, in order to make a valid comparison between the MNO and NMC, it is better to normalise the resistance for the electrochemically active surface area of each electrode. The exchange current density, calculated from the R_{ct} according to Eq. (6), is normalised for the active surface area and therefore makes for a better comparison.

The exchange current densities of MNO and NMC622 were calculated from GITT and are plotted in Fig. 5 c and Fig. 5 d, respectively. At 50 % SOC, the exchange current density $j_{0,a}$ was ~0.011 mA cm^{-2} for MNO, compared to a $j_{0,c}$ of 0.17 mA cm^{-2} for NMC622 at the same SOC.. These values are remarkably comparable to a recent study performed on Nb_2O_5 and NCA, which also found an order of magnitude difference between j_0 of the negative and positive electrodes [15]. Care must be taken in these comparisons however, as this order of magnitude difference may be due calculation differences, and specifically the surface area determination methods, which may be overestimating the electrochemically active surface area of the MNO electrode and/or underestimating that of the NMC electrode.

Furthermore, to determine the temperature dependency of R_{ct} and j_0, impedance measurements in potentiostatic mode (PEIS) were carried out at 0, 5, 15, 25, 30, and 40 °C with MNO||Li and NMC||Li half-cells;

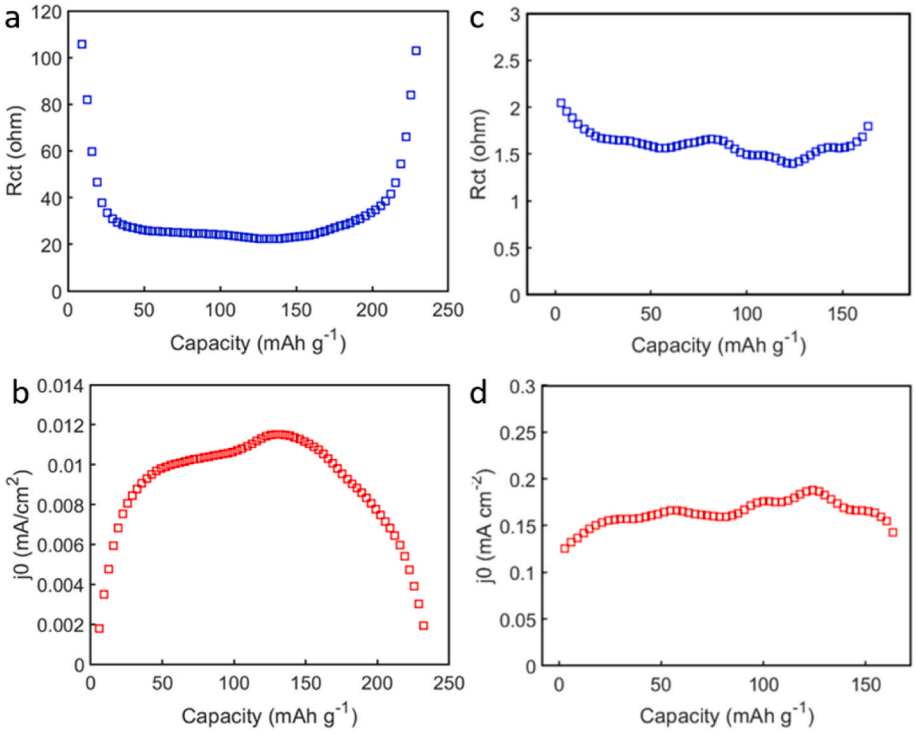

Fig. 5. Charge transfer resistance (R_{ct}) and exchange current density (j_0) of the MNO anode, $R_{ct,a}$ (a) and $j_{0,a}$ (b), and of the NMC cathode, $R_{ct,c}$ (c) and $j_{0,c}$ (d), calculated from the GITT data in half-coin cells.

the temperature and SOC dependency of these impedance measurements are shown in Fig. 7 and Fig. S4, respectively. The PEIS data of the MNO||Li cell was fitted to the equivalent circuit shown in Fig. 6 and the exchange current densities were thus calculated. Fig. 8 shows the fitting of PEIS data of MNO||Li at 25 °C and demonstrates that this equivalent circuit provided an excellent fit at all SOCs. Table 2 shows the R_{ct} values obtained at different temperature and their respective calculated j_0.

The equivalent electric circuit showed in Fig. 6 was used to fit the PEIS spectra recorded for the MNO||Li half-cell. It contains a serial ohmic resistor R_s in series with a first paralleled element containing a resistor R_{SEI} and a constant phase element Q_{SEI}, and finally another constant phase element Q_{dl} in parallel with a resistor R_{ct} that is in series with a constant phase element Q_{dif}. The PEIS analysis for the NMC622||Li half-cells, with the equivalent circuit and Nyquist plots, is provided in Fig. S4 in *Supplementary Information* and discussed briefly as the EIS of NMC cathodes has already been studied extensively elsewhere [41,42].

In the equivalent circuit of the MNO||Li, R_s corresponds to the series resistance associated with the internal ohmic resistance of the bulk materials and components in the cells, especially the electrolyte and the separator but also including the current collectors and electric contacts. These components do not have a capacitance or inductance associated with them and therefore the value of R_s can be deducted directly on the Re(Z) axis. R_{SEI} and Q_{SEI} respectively correspond to the interfacial resistance and capacitance associated with the presence of solid electrolyte interphase (SEI) layer at the surface of the working electrode which may slow the ionic transport at the electrode-electrolyte interface. R_{ct} on the other hand corresponds to the charge transfer resistance at the electrode-electrolyte interface, which is associated with the capacitive effects of the electrical double layer, captured by the constant phase element Q_{dl}. Finally, Q_{dif} represents the diffusion of the Li-ions within the active material lattice and into the bulk of the electrolyte phase, which is captured at the low frequency region of the EIS spectra (we do not use a Warburg element here as W should only be used for semi-infinite diffusion, while the diffusion tails of these batteries clearly had a capacitive and resistive effects associated to them and therefore Q makes more sense than W for the PEIS fitting).

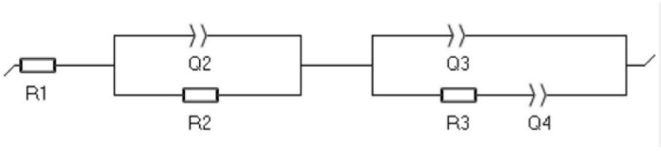

Fig. 6. Equivalent electric circuit diagram used to fit the PEIS data for MNO||Li half cells.

The EIS spectra of the MNO||Li half-cell appear to be mostly made of a single depressed semi-circle that spans the high and medium frequencies, and a diffusion tail at low frequencies, which progressively tapers off due to increased resistance as the SOC increases, Fig. 7(a and b). The semi-circle, which we attributed to the charge transfer process, ends at ~10 Hz at temperatures above 25 °C but is progressively shifted down to 1 Hz as the temperature decreases towards 0 °C, which points to a slow-down of the rate of the charge transfer process at low temperatures. This slow-down is clearly the result of increased resistance at the electrode-electrolyte interface at low temperature, which is also evidenced by the increasingly higher R_{ct} with decreasing temperature [32]. On the other hand, the R_{ct} also clearly decreases above 50 % SOC, as shown on the Nyquist plot of the PEIS at various temperatures at 80 % SOC (Fig. 7 c). This is further confirmed by the PEIS plots at 60 and 80 % SOC at 25 °C in Fig. 8. At the same time, in the low-frequency region, the length and height of the diffusion tail increases as the SOC increases from 20 % to 50 % and then 80 %, suggesting an increase of the resistance and capacitance associated with this process as the SOC increases. This is further confirmed in Fig. 8 where it becomes evident that the magnitude and shape of these semi-circles at 25 °C varies significantly between 0 % SOC (high voltage cut-off) and 100 % SOC (lower voltage cut-off). Indeed, what initially appears to be a Warburg element based on the straight diffusion tail at 0 % SOC progressively tappers off as the SOC increases, indicating that a resistance is associated with this slow diffusion process, to eventually form another depressed semi-circle at 100 % SOC. This different behaviour during EIS at 0 % and 100 % SOC is

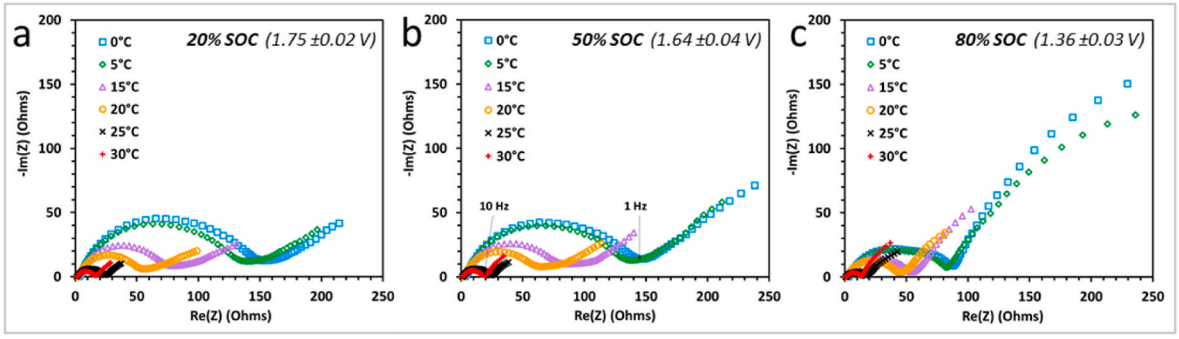

Fig. 7. Temperature dependency of PEIS in MNO||Li half cells between 0 °C and 30 °C at 20 % SOC (a), 50 % SOC (b), 80 % SOC (c).

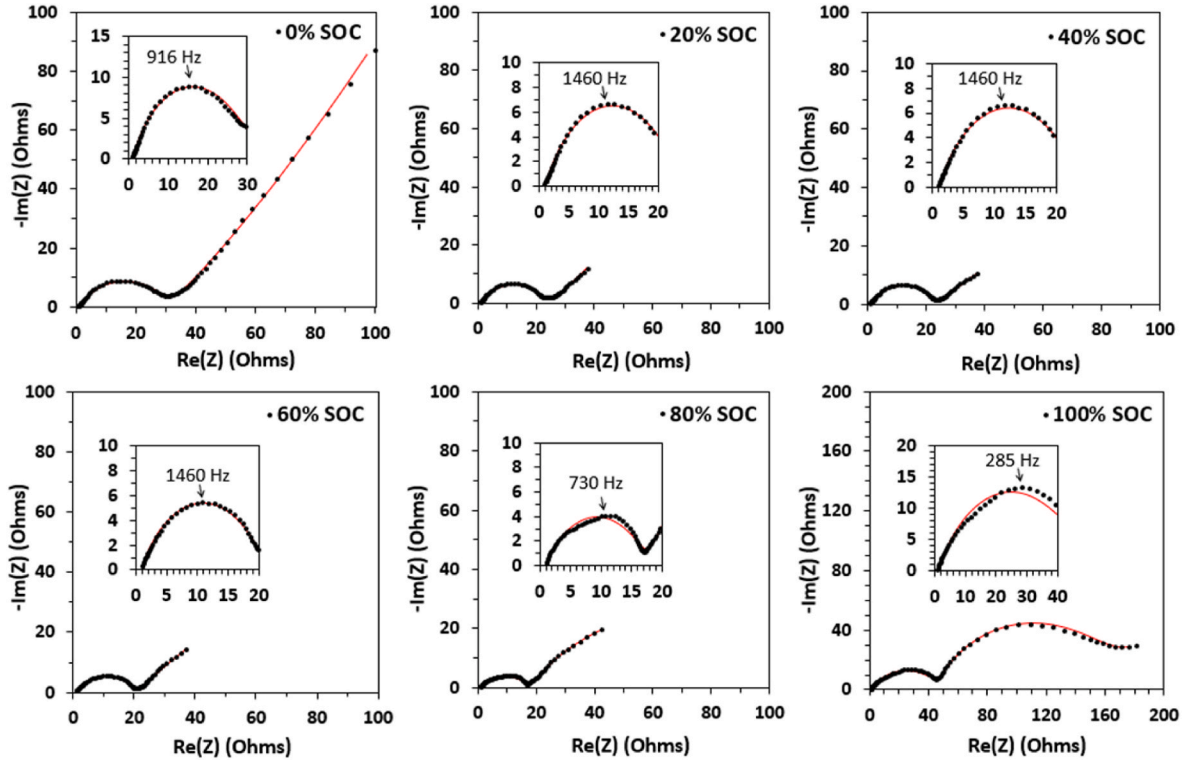

Fig. 8. Nyquist plot of the PEIS of an MNO||Li anode half-cell between 0 % and 100 % SOC in 20 % SOC increments. The fit (red lines on the plots) was performed using an R1+[Q2/R2]+[Q3/(R3+Q4)] equivalent circuit. (For interpretation of the references to colour in this figure legend, the reader is referred to the Web version of this article.)

Table 2
Series bulk resistance (Rb), charge transfer resistance (Rct), exchange current density (j0), and reaction rate (k) of MNO and NMC electrodes at 50 % SOC at various temperatures calculated from PEIS data.

Electrode			Temperature			
			5 °C	15 °C	25 °C	35 °C
MNO	R_b	(Ω)	2.5	1.9	0.94	0.93
	R_{ct}	(Ω)	152	97.9	22.49	26.81
	$j_{0,MNO}$	(mA cm^{-2})	0.0029	0.0046	0.0208	0.0180
	$k_{,MNO}$	(A m^{-2} (m^3 mol^{-1})$^{1.5}$)	3.75E-8	6.02E-8	2.71E-7	2.35E-7
NMC622	R_b	(Ω)	1.44	0.95	0.76	0.27
	R_{ct}	(Ω)	9.4	3.6	2.3	1.1
	$j_{0,NMC}$	(mA cm^{-2})	0.217	0.586	0.948	2.050
	$k_{,NMC}$	(A m^{-2} (m^3 mol^{-1})$^{1.5}$)	2.18E-6	5.89E-6	9.53E-6	2.06E-5

to be expected as battery electrodes typically experience significant polarisation effects at these states of charge, especially in half-cell, which bring it outside of the linear voltage region. Therefore, we assigned the second semi-circle at 100 % SOC to increased charge transfer resistance due to polarisation effects and overpotentials.

Finally, the inserts showing the high-to-medium frequency region of each Nyquist plot at 25 °C in Fig. 8 show that there is a change in the morphology of the semi-circle at 80 % and 100 % SOC compared to lower SOC, with the appearance of an interfacial resistance R_{SEI} at SOC >60 %, which may suggest the formation of a thicker SEI layer at the surface of the MNO particles below 1.6 V. This is further confirmed when analysing the frequency at which the top of the main semi-circle is reached, showing that the top is reached at 1460 Hz at 20, 40 and 60 % SOC but there is a shift to lower frequency (730 Hz) at 80 % SOC, indicating a slowdown of the ionic transport process due to increased interfacial resistance at the liquid/solid interphase. However, the fact that the semi-circle associated with R_{SEI} tends to increase above 70 % SOC and then nearly disappear throughout cycling below 70 % SOC

indicates that the SEI or SEI-like layer that forms at the surface of the MNO particles is likely thin and/or unstable, resulting in a weak energy barrier and low interfacial resistance for the Li ions to overcome during the intercalation process, and little to no effective Li consumption from SEI growth during cycling of the MNO.

The charge transfer resistance, exchange current density, and reaction rate of the negative and positive electrodes were also determined by fitting the experimental PEIS data obtained in half cells at various temperatures and SOCs. The values calculated for each of these parameters at 50 % SOC for both electrodes are shown in Table 2.

Both R_b and R_{ct} were significantly higher for the MNO than the NMC, which is consistent with the values extracted from GITT (Fig. 5). This trend was observed at all temperatures, whilst the expected increase of the resistances at low temperatures was also observed. The value of $j_{0,MNO}$ at 50 % SOC obtained from PEIS agreed well with that calculated from GITT though slightly higher at 0.019 mA cm^{-2} for the former compared to 0.012 mA cm^{-2} for the latter. Nevertheless, the general trend of exchange current density calculated at 0, 20, 40, 50, 80, and 100 % SOC, respectively, were in good agreement between GITT and EIS (Fig. S5 and Fig. S6 in *Supplementary Information*).

The reaction rate of MNO, k_{MNO}, ranged within 10^{-8}-10^{-7} A m^{-2} (m^3 mol^{-1})$^{1.5}$ whereas that of the NMC622, k_{NMC}, was higher at 10^{-7}-10^{-5} A m^{-2} (m^3 mol^{-1})$^{1.5}$, indicating that the negative electrode is the reaction-limited electrode.

Finally, the charge transfer reaction activation energy of $MoNb_{12}O_{33}$ ($E_{a,MNO}$) and of NMC622 ($E_{a,NMC}$) were determined from the slope of the Arrhenius plots at various SOCs (Fig. 4 and Fig. S6 in *Supplementary Information*) [43]. E_a was determined to be equivalent for MNO and NMC622 at 50 % SOC, being 50.3 and 51.6 kJ mol^{-1}, respectively. However, while these values remained relatively comparable in the range 0–50 % SOC, they deviated significantly at higher SOCs, with $E_{a,MNO}$ of 50.3 and 47.3 kJ mol^{-1} at 80 % and 100 % SOC, respectively, whilst $E_{a,NMC}$ increased to 72.6–83.2 kJ mol^{-1} above 75 % SOC. As expected from theory, the activation energy of MNO is approximately constant with concentration.

3.5. Rate performance of half-coin and full-coin cells at low temperatures

Temperature has a substantial impact on the rate performance of Li-ion batteries, which is typically negatively affected at low temperatures due to more sluggish ion transport through the electrolyte and the active material particles, slower interfacial Li-ion flux at the liquid/solid interphase, a slower reaction rate and higher potential hysteresis [38]. However it is challenging to decouple the contribution of the negative electrode from the positive electrode, as the lithium metal in half cells significantly influences the results. Fig. S7 in *Supplementary Information* displays the rate capability of a 1.1 mAh cm^2 MNO||Li anode *half-cell* at 25 °C, 15 °C, and 0 °C, upon asymmetric delithiation and lithiation, respectively. First, the difference between the delithiation and lithiation rate performance is evident at all temperatures, with much higher capacity retention at high rates upon delithiation (half-cell charge) than during lithiation (half-cell discharge). This is consistent with results previously reported with this material in half-cells, and full-cells should not be expected to display the same shortcomings [21]. The ultrahigh delithiation rate performance of this half-cell is outstanding at 25 °C, with 90 % and 64 % capacity retention at 10C and 20C, respectively, compared with the capacity at 1C. There was a sharp drop in capacity retention at those same ultrahigh rates at 15 °C, with only 60 mAh g^{-1} being obtained at 10C compared to 180 mAh g^{-1} at 10C at 25 °C, while a 20C delithiation rate yielded 130 mAh g^{-1} at 25 °C but 0 mAh g^{-1} at 15 °C. Nevertheless, the low-rate and high-rate performance of half-cells remained excellent at 15 °C, with merely 5–10 % difference compared to the capacity at 25 °C with current rates up to 2C, and only a 16 % difference at 5C. However, little to no capacity could be extracted at rates ≥ 5C at 0 °C, although this issue was not observed in full cells, as discussed in the next section. Nevertheless, the 2C capacity at 0 °C remained appreciable, yielding 150 mAh g^{-1}, which is 75 % of the 2C capacity at 25 °C.

The rate capability of an NMC622||MNO *full cell* was also characterised from 0.1C to 20C at the same three temperatures, and the resulting voltage profiles are plotted in Fig. 9. First, the issue with poor capacity retention at high rates upon lithiation of the MNO anode in half-cell was not observed in full cells. Instead, in full cells, the capacity retention at all rates was nearly identical in charge and discharge at all temperatures, as evidenced in Fig. 9. This difference in high rate performance in half and full cells was expected based on previous electrochemical testing of this material, indicating that the limitations observed in half-cell are due to the lithium metal electrode stripping and plating at high rates [21]. Furthermore, the percentage of capacity retention was higher in full cells than in half cells at all rates, and there was also significantly less capacity fade at high and ultrahigh rates at low temperatures in full cells. Indeed, a 20C charge of NMC622||MNO full-cells, starting from 0 % SOC, yielded 75 % capacity at 25 °C and 65 % SOC at 15 °C, whilst 75 % of the capacity could be achieved in 6 min at 15 °C using a 10C current rate. Although the internal resistances measured by PEIS in full cell increased significantly at low temperatures (Fig. 10), the rate performance of NMC622||MNO remained outstanding at 0 °C, as a 2C charging rate provided 75 % capacity. Furthermore, a 5C charge at 0 °C provided as much as 65 % capacity, whilst a 10C charge (6 min) yielded 50 % capacity in full cells. These results confirm that the lower performance at 0 °C in half-cell is likely caused by exacerbated lithium stripping and plating at low temperature due to the use of Li metal as the negative electrode.

The capacity retention of this $MoNb_{12}O_{33}$ electrode at high current rates is much greater than that of half cells and full cells based on $NiNb_2O_6$ electrodes reported in the literature [40]. Indeed, the $NiNb_2O_6$ displayed a capacity retention at 10C compared to 1C of 64 % in half cell and only 31 % in NMC811||$NiNb_2O_6$ full cell, whereas the present $MoNb_{12}O_{33}$ electrode provided 89 % capacity retention on charge in both half and full cells.

Furthermore, few low temperature charge and discharge rate results of niobium oxide-based Li-ion cells have been reported to date in peer-reviewed publications. One study of an $LiNi_{0.5}Mn_{1.5}O_4$|| $Al_{0.5}Nb_{24.5}O_{62}$ cell that reported only the discharge rate at 0 °C with much lower performance than the present study, while using significantly higher carbon black loadings and a 75 % lower active mass loading in their electrodes [8]. Niobium tungsten oxide $Nb_{16}W_5O_{55}$ was shown to experience significant specific capacity loss and relatively poor rate performance at low temperatures (0 and −20 °C) in half-cell [44], It also displayed inferior capacity retention at 10 °C in NMC622||NWO full cells, with a ~22 % specific capacity loss at 2C and ~71 % lower capacity at 10C [45].

The superior rate performance of the molybdenum niobate material in the current study can be explained in part by its significantly higher solid diffusion coefficient (Fig. 4) as well as lower bulk and solid-state resistances (Fig. 8), which may be due to the various particle engineering modifications done by the manufacturer, including doping strategy, carbon coating morphology, and control of the particle size distribution [15,20]

The Nyquist and Bode plots of an NMC622||MNO full cell after formation at various temperatures between 40 °C and 0 °C are displayed in Fig. 10a and Fig. 10 b, respectively. All the Nyquist spectra are clearly made up of a first small semi-circle at high frequencies; followed by a bigger yet incomplete second semi-circles at medium frequencies; and finally, a diffusion tail at high frequencies.

First, the ohmic series resistance R_s of the full cell remains identical between 40 and 15 °C, well below 1 Ω. However, R_s increases to above 1 Ω at 5 °C and reaches 2 Ω at 0 °C. This resistance increase, although relatively small in absolute terms, remains significant in % terms and likely contributes somehow to lowering the high-rate performance of the NMC622||MNO cell at 0 °C.

The diameter of the first semi-circle at high frequencies is mostly

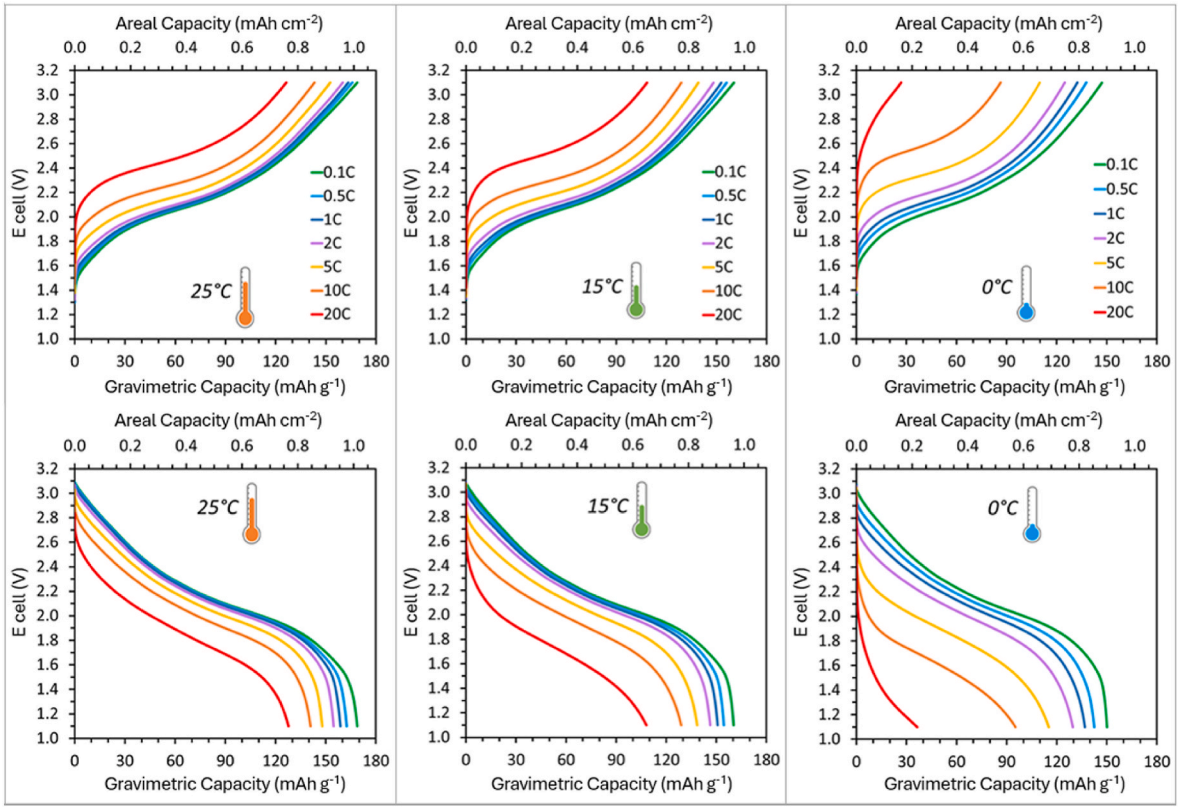

Fig. 9. Rate capability of NMC622||MNO full coin cells at 25 °C, 15 °C, and 0 °C showing the outstanding rate performance of these battery cells on both charge (top) and discharge (bottom) even at low temperatures. NMC622||MNO full cells were cycled between 1.1 and 3.1 V. The fixed low-rate discharge/charge applied during these asymmetric charging and discharging rate tests, respectively, were CCCV profiles at 0.5C with 0.05C cut-off (not shown on these graphs). Voltages are expressed vs. Li/Li^+.

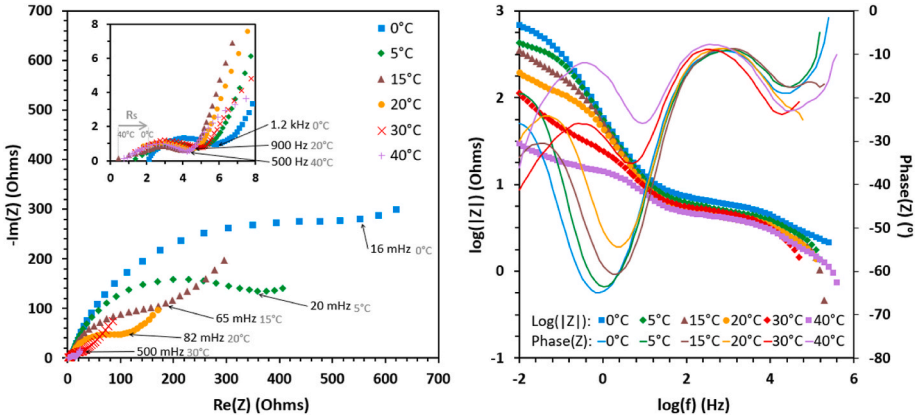

Fig. 10. Nyquist plot (left) and Bode plot (right) from the PEIS of an NMC622||MNO full coin cell between 0 °C and 40 °C. PEIS was performed using a 5 mV amplitude between 400 kHz and 10 mHz at each temperature.

unaffected by the temperature decrease, and the frequencies associated with this semi-circle remain identical at all temperatures, which points to very little impact of temperature on the resistance and rate of the associated process in full cell. The fact that high-rate processes were not substantially affected by temperature in full cell may partially explain why full cells retained their high-rate performance at low temperature much better than half-cells. Furthermore, it is important to note that much smaller resistances are observed overall in full cell than in half cell at all temperatures, which also supports the fact that full cells would display better rate performance than half-cells.

However, the R_{ct} – represented by the diameter of the second semi-circle at higher frequencies – increased substantially as the temperature decreased. Finally, the low frequency response, which is ascribed to the diffusion of the ionic species in the host materials lattices and in the electrolyte, displayed the expected trend of increased ionic transport resistance with decreasing temperature. Furthermore, the frequency at which the diffusion tail starts is progressively shifted to lower frequencies with decreasing temperatures. This resistance increase and frequency shift were substantial and explain in part the lower rate performance with falling temperatures from 25 °C to 0 °C, especially at very high rates (10C and 20C) at 0 °C where bulk diffusion is highly impeded by R_{dif} that is nearly one order of magnitude higher than at 20 °C.

Diffusion coefficients are measured at low current densities, and the

negative electrode has significantly lower current densities than the cathode, indicating that the rate kinetics are much slower in the negative electrode than the positive, at an electrode level. However, these are recorded in a half cell configuration, where at higher current densities the lithium stripping and plating on the counter electrode may cause a greater kinetics limitation than occurs at the working electrode. In a full cell configuration, we can observe that good rates are possible, we can assume that the a potential cause of rate limitation is likely to occur at the positive electrode because of the slow diffusion coefficient we have observed, however higher overpotentials may be observed at the negative electrode because of the high exchange current densities and over potentials measure, indicating slower reaction rates. In every full cell system, there is a balance between ionic and electronic transport properties. To improve the electrode and cell rate further, these results suggest that the particle size of the positive electrode should be reduced, and potentially some surface modification of the negative electrode would improve the kinetics at the surface.

4. Conclusions

In this work, we characterised and tested lithium-ion battery cells based on an $MoNb_{12}O_{33}$ (MNO) molybdenum niobium oxide anode and an NMC 622 cathode. Asymmetric charge and discharge rate tests at high current rates and low temperatures in half-cell and full cell, as well as GITT and PEIS, provide a comprehensive overview of the kinetics and thermodynamics of the Li-ion insertion/extraction mechanisms in these electrodes.

From GITT experiments, the MNO had an exchange current density of ~0.012 mA cm^{-2} at 50 % SOC and a high apparent Li diffusion coefficient of $\sim 10^{-9}$ cm^2 s^{-1}. The analysis of PEIS data at 25 °C yielded an exchange current density of 0.019 mA cm^{-2} at 50 % SOC and a reaction rate of 2.49 10^{-7} A m^{-2} $(m^3\ mol^{-1})^{1.5}$ and a charge transfer reaction Arrhenius activation energy of 50 ± 2.7 kJ mol^{-1}. Niobium oxides are typically believed to not form an SEI layer at all due to having a potential above 1.0V. However, PEIS results in this study suggested the possible formation of an unstable or reversible SEI layer at the surface of the MNO, with the emergence of an additional impedance contribution during EIS at 70–100 % SOC.

Lithiation and delithiation rate tests at 15 °C and 0 °C highlighted the exceptional rate performance of this MNO anode material even at low temperatures using a liquid organic electrolyte. Indeed, NMC622||MNO full cells could be charged and discharged from 0 to 75 % capacity in 3 min using a 20C current rate at 25 °C and in 6 min using 10C rate at 15 °C. Despite the increased impedance, charge transfer resistance, and reaction rate measured by PEIS at low temperatures, the rate performance of NMC622||MNO full cells remained outstanding at 0 °C as they could be charged from 0 to 75 % in 30 min using a 2C current rate, while a 6 min charge (10C rate) at 0 °C still provided 50 % capacity. These results highlight the superior rate performance of $MoNb_{12}O_{33}$-based batteries over graphite-based batteries even at low temperatures.

Future works may use the parameter dataset with validation data from this study in further DFN modelling and simulation studies. It would also be useful to investigate the effect of higher electrode active mass loadings (3–5 mAh cm^{-2}) on the rate capability and cycling performance of cells using Wadsley-Roth niobium oxides, to better define the electrode and cell design boundaries for power cells and energy cells, respectively.

Data statement

The raw dataset from this study is available from Prof Emma Kendrick upon reasonable request.

CRediT authorship contribution statement

Yazid Lakhdar: Methodology, Formal analysis, Writing – original draft, Writing – review & editing. **Yongxiu Chen:** Formal analysis, Writing – review & editing. **Harry Geary:** Writing – review & editing. **Maurits E. Houck:** Writing – review & editing. **Alexander S. Groombridge:** Writing – review & editing, Writing – review & editing. **Peter R. Slater:** Project administration, Writing – review & editing. **Emma Kendrick:** Conceptualization, Methodology, Project administration, Writing – review & editing.

Declaration of competing interest

The authors declare the following financial interests/personal relationships which may be considered as potential competing interests: Harry Geary, Maurits E. Houck, and Alexander S. Groombridge are employees of Echion Technologies Ltd, which develop niobium-based materials for energy storage applications.

Data availability

Data will be made available on request.

Acknowledgements

We acknowledge the funding support received from Innovate UK Faraday Battery Challenge SUPERB project (grant number 250619) and the Faraday Institution NEXTRODE project (faraday.ac.uk; EP/S003053/1, FIRG015) and CATMAT project (FIRG016). We also acknowledge the technical support provided by QinetiQ during the duration of the SUPErB project.

Appendix A. Supplementary data

Supplementary data to this article can be found online at https://doi.org/10.1016/j.jpowsour.2023.233710.

References

[1] International Energy Agency (IEA), Global EV outlook 2022 - securing supplies for an electric future, Glob. EV Outlook 2022 (2022) 221.
[2] Y. Yang, J. Zhao, Wadsley–roth crystallographic shear structure niobium-based oxides: promising anode materials for high-safety lithium-ion batteries, Adv. Sci. 8 (12) (2021) 1–24, https://doi.org/10.1002/advs.202004855.
[3] L. Hu, L. Luo, L. Tang, C. Lin, R. Li, Y. Chen, Ti2Nb2: XO4+5 x anode materials for lithium-ion batteries: a comprehensive review, J. Mater. Chem. A 6 (21) (2018) 9799–9815, https://doi.org/10.1039/c8ta00895g.
[4] R.J. Cava, D.W. Murphy, S.M. Zahurak, Lithium insertion in wadsley-roth phases based on niobium oxide, J. Electrochem. Soc. 130 (12) (1983) 2345–2351, https://doi.org/10.1149/1.2119583.
[5] C.P. Koçer, K.J. Griffith, C.P. Grey, A.J. Morris, Cation disorder and lithium insertion mechanism of wadsley-roth crystallographic shear phases from first principles, J. Am. Chem. Soc. 141 (38) (2019) 15121–15134, https://doi.org/10.1021/jacs.9b06316.
[6] J.T. Han, Y.H. Huang, J.B. Goodenough, New anode framework for rechargeable lithium batteries, Chem. Mater. 23 (8) (2011) 2027–2029, https://doi.org/10.1021/cm200441h.
[7] Q. Cheng, J. Liang, Y. Zhu, L. Si, C. Guo, Y. Qian, Bulk Ti2Nb10O29 as long-life and high-power Li-ion battery anodes, J. Mater. Chem. A 2 (41) (2014) 17258–17262, https://doi.org/10.1039/c4ta04184d.
[8] Q. Fu, R. Li, X. Zhu, G. Liang, L. Luo, Y. Chen, C. Lin, X.S. Zhao, Design, synthesis and lithium-ion storage capability of Al0.5Nb24.5O62, J. Mater. Chem. A 7 (34) (2019) 19862–19871, https://doi.org/10.1039/c9ta04644e.
[9] H. Yu, J. Zhang, R. Zheng, T. Liu, N. Peng, Y. Yuan, Y. Liu, J. Shu, Z.B. Wang, The journey of lithium ions in the lattice of PNb9O25, Mater. Chem. Front. 4 (2) (2020) 631–637, https://doi.org/10.1039/c9qm00694j.
[10] D. Saritha, V. Pralong, U.V. Varadaraju, B. Raveau, Electrochemical Li insertion studies on WNb12O33-A shear ReO3 type structure, J. Solid State Chem. 183 (5) (2010) 988–993, https://doi.org/10.1016/j.jssc.2010.03.003.
[11] F. Ran, X. Cheng, H. Yu, R. Zheng, T. Liu, X. Li, N. Ren, M. Shui, J. Shu, Nanostructured GeNb18O47 as novel anode host with superior lithium storage performance, Electrochim. Acta 282 (2018) 634–641, https://doi.org/10.1016/j.electacta.2018.06.109.
[12] C. Yang, S. Yu, C. Lin, F. Lv, S. Wu, Y. Yang, W. Wang, Z.Z. Zhu, J. Li, N. Wang, S. Guo, Cr0.5Nb24.5O62 nanowires with high electronic conductivity for high-rate and long-life lithium-ion storage, ACS Nano 11 (4) (2017) 4217–4224, https://doi.org/10.1021/acsnano.7b01163.

[13] X. Lou, R. Li, X. Zhu, L. Luo, Y. Chen, C. Lin, H. Li, X.S. Zhao, New anode material for lithium-ion batteries: aluminum niobate (AlNb 11 O 29), ACS Appl. Mater. Interfaces 1–8 (2019), https://doi.org/10.1021/acsami.8b20246.
[14] Matthew W. Logan, Dajie Zhang, Bing Tana, Konstantinos Gerasopoulos, A scalable aluminum niobate anode for high energy, high power practical lithium-ion batteries, J. Mater. Chem. A 9 (2021) 11228–11240, https://doi.org/10.1039/D1TA00613D.
[15] Maurits E. Houck, Alexander S. Groombridge, Michael F.L. De Volder, Adam M. Boies, Parameterization and modeling protocols for ultra-fast charging Wadsley-Roth lithium-ion batteries from coin to pouch cells, Cell Reports Physical Science 4 (2023), 101410, https://doi.org/10.1016/j.xcrp.2023.101410.
[16] X. Zhu, J. Xu, Y. Luo, Q. Fu, G. Liang, L. Luo, Y. Chen, C. Lin, X.S. Zhao, MoNb12O33 as a new anode material for high-capacity, safe, rapid and durable Li + storage: structural characteristics, electrochemical properties and working mechanisms, J. Mater. Chem. A 7 (11) (2019) 6522–6532, https://doi.org/10.1039/c9ta00309f.
[17] O.A. Drozhzhin, M.A. Vorotyntsev, S.R. Maduar, N.R. Khasanova, A.M. Abakumov, E.V. Antipov, Li-ion diffusion in LixNb9PO25, Electrochim. Acta 89 (2013) (2013) 262–269, https://doi.org/10.1016/j.electacta.2012.11.017.
[18] K.J. Griffith, K.M. Wiaderek, G. Cibin, L.E. Marbella, C.P. Grey, Niobium tungsten oxides for high-rate lithium-ion energy storage, Nature 559 (7715) (2018) 556–563, https://doi.org/10.1038/s41586-018-0347-0.
[19] H. Yu, J. Zhang, M. Xia, C. Deng, X. Zhang, R. Zheng, S. Chen, J. Shu, Z.B. Wang, PNb9O25 nanofiber as a high-voltage anode material for advanced lithium ions batteries, J. Mater. 6 (4) (2020) 781–787, https://doi.org/10.1016/j.jmat.2020.07.003.
[20] A.S. Groombridge, J. D. La Verpilliere, S. Santhanam, W. Zhang, M.E. Houck, Li/Na-Ion Battery Anode Materials, GB-2588254-A, 2021.
[21] Y. Lakhdar, H. Geary, M. Houck, D. Gastol, A.S. Groombridge, P.R. Slater, E. Kendrick, Optimization of electrode and cell design for ultrafast-charging lithium-ion batteries based on molybdenum niobium oxide anodes, ACS Appl. Energy Mater. (2022), https://doi.org/10.1021/acsaem.2c01814.
[22] M.J. Lain, J. Brandon, E. Kendrick, Design strategies for high power vs. High energy lithium ion cells, Batteries 5 (4) (2019), https://doi.org/10.3390/batteries5040064.
[23] C.-H. Chen, F. Brosa Planella, K. O'Regan, D. Gastol, W.D. Widanage, E. Kendrick, Development of experimental techniques for parameterization of multi-scale lithium-ion battery models, J. Electrochem. Soc. 167 (8) (2020), 080534, https://doi.org/10.1149/1945-7111/ab9050.
[24] W. Weppner, R.A. Huggins, Determination of the kinetic parameters of mixed-conducting electrodes and application to the system Li3Sb, J. Electrochem. Soc. 124 (10) (1977) 1569–1578, https://doi.org/10.1149/1.2133112.
[25] Y. Chen, J. Key, K. O'Regan, T. Song, Y. Han, E. Kendrick, Revealing the rate-limiting electrode of lithium batteries at high rates and mass loadings, Chem. Eng. J. 450 (3) (2022), 138275.
[26] A.A. Wang, S.E.J. O'Kane, F. Brosa Planella, J. Le Houx, K. O'Regan, M. Zyskin, J. Edge, C.W. Monroe, S.J. Cooper, D.A. Howey, E. Kendrick, J.M. Foster, Review of parameterisation and a novel database (LiionDB) for continuum Li-ion battery models, Prog. Energy 4 (3) (2022), https://doi.org/10.1088/2516-1083/ac692c.
[27] A. Verma, K. Smith, S. Santhanagopalan, D. Abraham, K.P. Yao, P.P. Mukherjee, Galvanostatic intermittent titration and performance based analysis of LiNi 0.5 Co 0.2 Mn 0.3 O 2 cathode, J. Electrochem. Soc. 164 (13) (2017) A3380–A3392, https://doi.org/10.1149/2.1701713jes.
[28] F. Xin, H. Zhou, Y. Zong, M. Zuba, Y. Chen, N.A. Chernova, J. Bai, B. Pei, A. Goel, J. Rana, F. Wang, K. An, L.F.J. Piper, G. Zhou, M.S. Whittingham, What is the role of Nb in nickel-rich layered oxide cathodes for lithium-ion batteries? ACS Energy Lett. 6 (4) (2021) 1377–1382, https://doi.org/10.1021/acsenergylett.1c00190.
[29] A. Ehrl, J. Landesfeind, W.A. Wall, H.A. Gasteiger, Determination of transport parameters in liquid binary lithium ion battery electrolytes, J. Electrochem. Soc. 164 (4) (2017) A826–A836, https://doi.org/10.1149/2.1131704jes.
[30] S.G. Stewart, J. Newman, The use of UV/vis absorption to measure diffusion coefficients in LiPF6 electrolytic solutions, J. Electrochem. Soc. 155 (1) (2008) F13, https://doi.org/10.1149/1.2801378.
[31] H. Lundgren, M. Behm, G. Lindbergh, Electrochemical characterization and temperature dependency of mass-transport properties of LiPF6 in EC:DEC, J. Electrochem. Soc. 162 (3) (2015) A413, https://doi.org/10.1149/2.0641503jes.
[32] J. Landesfeind, T. Hosaka, M. Graf, K. Kubota, S. Komaba, H.A. Gasteiger, Comparison of ionic transport properties of non-aqueous lithium and sodium hexafluorophosphate electrolytes, J. Electrochem. Soc. 168 (4) (2021), 040538, https://doi.org/10.1149/1945-7111/abf8d9.
[33] X.Y. Qiu, Q.C. Zhuang, Q.Q. Zhang, R. Cao, Y.H. Qiang, P.Z. Ying, S.G. Sun, Investigation of layered LiNi1/3Co 1/3Mn1/3O2 cathode of lithium ion battery by electrochemical impedance spectroscopy, J. Electroanal. Chem. 688 (2013) 393–402, https://doi.org/10.1016/j.jelechem.2013.02.009.
[34] V.J. Ovejas, A. Cuadras, Impedance characterization of an LCO-NMC/graphite cell: ohmic conduction, sei transport and charge-transfer phenomenon, Batteries 4 (3) (2018), https://doi.org/10.3390/batteries4030043.
[35] Zhengyu Ju, Xiao Zhang, Jingyi Wu, Steven T. King, Chung-Chueh Chang, Shan Yan, Xue Yuan, Kenneth J. Takeuchi, Amy C. Marschilok, Lei Wang, Esther S. Takeuchi, Guihua Yu, Tortuosity engineering for improved charge storage kinetics in high-areal-capacity battery electrodes, Nano Lett. 22 (16) (2022) 6700–6708, https://doi.org/10.1021/acs.nanolett.2c02100.
[36] J. Landesfeind, J. Hattendorff, A. Ehrl, W.A. Wall, H.A. Gasteiger, Tortuosity determination of battery electrodes and separators by impedance spectroscopy, J. Electrochem. Soc. 163 (7) (2016) A1373–A1387, https://doi.org/10.1149/2.1141607jes.
[37] N. Ogihara, S. Kawauchi, C. Okuda, Y. Itou, Y. Takeuchi, Y. Ukyo, Theoretical and experimental analysis of porous electrodes for lithium-ion batteries by electrochemical impedance spectroscopy using a symmetric cell, J. Electrochem. Soc. 159 (7) (2012) A1034–A1039, https://doi.org/10.1149/2.057207jes.
[38] I.V. Thorat, D.E. Stephenson, N.A. Zacharias, K. Zaghib, J.N. Harb, D.R. Wheeler, Quantifying tortuosity in porous li-ion battery materials, J. Power Sources 188 (2) (2009) 592–600, https://doi.org/10.1016/j.jpowsour.2008.12.032.
[39] T.-T. Nguyen, A. Demortière, B. Fleutot, B. Delobel, C. Delacourt, S.J. Cooper, The electrode tortuosity factor: why the conventional tortuosity factor is not well suited for quantifying transport in porous Li-ion battery electrodes and what to use instead, Npj Comput, Materials 6 (1) (2020) 123, https://doi.org/10.1038/s41524-020-00386-4.
[40] Rui Xia, Kangning Zhao, Jie Zheng, Tao Shen, Lei Zhang, Mark Huijben, Johan ten Elshof, Decoupling reaction rate and diffusion limitation to fast-charging electrodes by extended modeling of cyclic voltammetry data, Energy Storage Mater. 53 (2022) 381–390.
[41] B. Babu, M.M. Shaijumon, Studies on kinetics and diffusion characteristics of lithium ions in TiNb2O7, Electrochim. Acta 345 (2020), 136208, https://doi.org/10.1016/j.electacta.2020.136208.
[42] R. Xia, K. Zhao, L.Y. Kuo, L. Zhang, D.M. Cunha, Y. Wang, S. Huang, J. Zheng, B. Boukamp, P. Kaghazchi, C. Sun, J.E. ten Elshof, M. Huijben, Nickel niobate anodes for high rate lithium-ion batteries, Adv. Energy Mater. 12 (1) (2022) 1–11, https://doi.org/10.1002/aenm.202102972.
[43] E.M. Gavilán-Arriazu, M.P. Mercer, O.A. Pinto, O.A. Oviedo, D.E. Barraco, H. E. Hoster, E.P.M. Leiva, Effect of temperature on the kinetics of electrochemical insertion of Li-ions into a graphite electrode studied by kinetic Monte Carlo, J. Electrochem. Soc. 167 (39) (2020), 013533.
[44] Xiao-Hang Ma, Xian Cao, Yuan-Yuan Ye, Qiao Fan, Men-Fa Qian, Yi-Yong Wei, Yao-Dong Wu, Zhen-Fa Zi, Jian-Ming Dai, Study on low-temperature performances of Nb16W5O55 anode for lithium-ion batteries, Solid State Ionics 353 (2020), 115376, https://doi.org/10.1016/j.ssi.2020.115376. ISSN 0167-2738.
[45] Yumi Kim, Quentin Jacquet, Kent J. Griffith, Jeongjae Lee, Sunita Dey, L. Bernardine, D. Rinkel, Clare P. Grey, High rate lithium ion battery with niobium tungsten oxide anode, J. Electrochem. Soc. 168 (2021), 010525, https://doi.org/10.1149/1945-7111/abd919.